

A “Flexible” Rigid Rod, *trans*-Pt(PMe₃)₂(C≡CC₆H₄CN)₂ (L1), to Form 2D [$\{\text{Cu}_2(\mu_2\text{-X})_2\}_2(\mu_4\text{-L1})\}_n$ Polymers (X = Br, I) Exhibiting the Largest Bathochromic Emissions

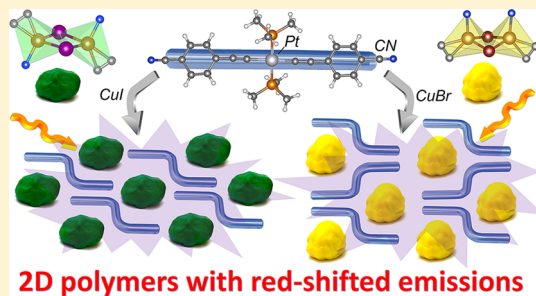
Frank Juvenal, Daniel Fortin,[✉] and Pierre D. Harvey*[✉]

Département de Chimie, Université de Sherbrooke, Sherbrooke, Québec J1K 2R1, Canada

S Supporting Information

ABSTRACT: The *trans*-Pt(PMe₃)₂(C≡CC₆H₄CN)₂ organometallic ligand L1, which is prepared from 4-ethynylbenzonitrile and *cis*-Pt(PMe₃)₂Cl₂, binds CuX salts to form two strongly luminescent two-dimensional coordination polymers (CPs) [$\{\text{Cu}_2(\mu_2\text{-X})_2\}_2(\mu_4\text{-L1})\}_n$ (X = I, CP1; X = Br, CP2). The emission quantum yields, $\Phi_e \approx 30\%$ at 298 K, are the largest ones for all CPs built upon the *trans*-Pt(PMe₃)₂(C≡CC₆H₄X)₂ motifs (X = SMe, CN). X-ray crystallography reveals that, to accommodate these layered CPs, L1 must undergo major distortions of the C≡C–C angles ($\sim 159^\circ$) and significant rotations about the Pt–CC bonds, so that the dihedral angles made by the two aromatic planes is 90° in a quasi-identical manner for both CPs. Together, these two features

represent the largest distortion for *trans*-Pt(PMe₃)₂(C≡CC₆H₄X)₂ complexes among all of the CPs built upon this type of ligand (2 of 16 entries). Concurrently, CP1 and CP2 also exhibit the most red-shifted emissions ($\lambda_{\text{max}} = 650$ and 640 nm, respectively) known for this type of chromophore at room temperature. The $\{\text{Cu}_2(\mu_2\text{-X})_2\}$ rhomboids adopt the *trans*- (X = I, common) and *cis*-geometries (X = Br, extremely rare) making them “isomers” if excluding the fact that the halides are different. Density functional theory (DFT) and time-dependent DFT suggest that the triplet emissive excited state is metal/halide-to-ligand charge transfer in both cases despite this difference in rhomboid geometry.



INTRODUCTION

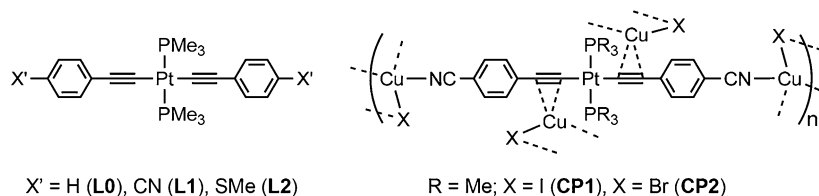
The use of organometallic ligands¹ for the formation of bimetallic coordination polymers (CPs),² metal-organometallic framework (MOMF),³ and two-dimensional (2D) nanoparticle network⁴ has been the topic of recent interest for applications in gas storage and sensors, catalysis, and optoelectronics. Difunctionalized ferrocenyls and metallocenes are classic fragments for the design of such heterobimetallic materials.⁵ Conversely, the so-called “rigid rod” and generally luminescent *trans*-Pt(PR₃)₂(C≡CCAr)₂ synthon ([Pt], R = alkyl, Ar = aromatic) is well-known for the design of one-dimensional (1D) organometallic polymers with applications in liquid crystals,⁶ nonlinear optics (including up conversion, two-photon absorption, and optical power limiting),⁷ light-emitting diodes,⁸ and solar cells.⁹ Recently, our group reported the use of a novel [Pt]-containing organometallic ligand, *trans*-Pt(PMe₃)₂(C≡CC₆H₄SMe)₂ (see L2 in Chart 1), which exhibits two coordination sites ($\eta^2\text{-C}\equiv\text{C}$ and S), for the formation of luminescent 1D and 2D CPs with CuX salts (X = Cl, Br, I).¹⁰ The common features are first, when Cu–S linkages are used in the coordination network, a 2D CP is systematically generated. This observation is entirely consistent that only 1D CPs are obtained with L0 (Chart 1).^{2b,c} Second, the coordination of either the resulting rhomboid Cu₂X₂ (X = Cl, Br, I) or staircase Cu₄I₄ secondary building units (SBUs) induce sensitive distortions of the [Pt] skeleton, and the formation of a charge transfer emissive triplet excited state

defined as a mixed excited state including intraligand-L2 ($\pi\pi^*$ / ligand-to-metal charge transfer (LMCT; i.e., C₆H₄C≡C → Pt)) and metal-to-ligand charge transfer (MLCT; M = Cu₂X₂ or Cu₄I₄; L = L2). Their emission bands exhibit maxima ranging from 570 to 605 nm, which are significantly red-shifted in comparison with that for L2 when not coordinated (476 and vibronic peak at 511 nm). When X = Br and Cl, only rhomboid SBUs are formed along with mainly 1D CPs (but not exclusively). Several questions remain; (1) can 2D CPs be obtained when using a N-donor linkers, (2) why some 2D CPs exhibit cavities available for crystallization molecules, while others do not have sufficient space to create solvent sites, and finally (3) is there a structure–property relationship that explains why these emissions are so red-shifted compared to the uncoordinated ligands?

We now report the synthesis and characterization of CP1 and CP2 exhibiting formula [$\{\text{Cu}_2(\mu\text{-X})_2\}_2(\mu_4\text{-L1})\}_n$, which answer these questions. During the course of this investigation, two new features are discovered. First, the emission maxima are the most red-shifted ones in the [Pt]-containing CPs ($\lambda_{\text{max}} = 650$ nm and extending well above 800 nm), and second, the Cu₂X₂ SBUs present both the *trans*- (X = I) and *cis*- (X = Br) geometries, making CP1 and CP2 “isomeric” materials. The latter form is rare and relies on bridging ligands.¹¹

Received: April 3, 2018

Chart 1. Structures of the [Pt]-Containing Organometallic Ligands and CPs



EXPERIMENTAL SECTION

Materials. 4-Bromobenzonitrile, trimethylsilylacetylene, triethylamine, and tetrahydrofuran (THF) were purchased from Sigma-Aldrich and were used as received without further purification except THF, which was distilled before use.

4-Ethynylbenzonitrile. 4-Bromobenzonitrile (5.214 g, 28.6 mmol), trimethylsilylacetylene (5.8 mL, 40.8 mmol), THF (35 mL), triethylamine (35 mL), PdCl₂(PPh₃)₂ (0.330 g, 0.470 mmol), and CuI (0.054 g, 0.284 mmol) were placed in a round-bottom flask, and the mixture was stirred under argon at 50 °C for 24 h. The reaction mixture was cooled at room temperature, and the solvent was removed on the rotovap. Purification was done by column chromatography on silica gel (CHCl₃/hexane: 1:7, v/v). Yield: 96%. The deprotection of the product was done using K₂CO₃ (10.60 g, 78.0 mmol) in MeOH/THF (45 mL/45 mL) and stirring the mixture overnight. The solution was filtrated, and the solvent was removed on the rotovap. The final solid product was further dried under a vacuum. Yield: 69%. ¹H NMR (300 MHz, CDCl₃) δ 7.62 (d, J = 8.6 Hz, 2H), 7.57 (d, J = 8.6 Hz, 2H), 3.30 (s, 1H).

Synthesis of the trans-Bis(4-ethynylbenzonitrile)bis(trimethylphosphine)platinum(III) ligand (L1). 4-cis-Dichlorobis(trimethylphosphine)platinum(II) (0.81 g, 1.9 mmol) and ethynylbenzonitrile (0.62 g, 0.49 mmol) were added in a degassed solution of Et₃NH (90 mL) placed in round-bottom flask, and CuI (6 mg, 0.03 mmol) was added to the mixture. The reaction mixture was stirred at 50 °C for 24 h. The solid was washed with cold water and cold methanol. Yield: 76%. ¹H NMR (300 MHz, CDCl₃) δ 7.49 (d, J = 8.3 Hz, 4H), 7.34 (d, J = 8.3 Hz, 4H), 1.83–1.67 (m, 18H). ³¹P NMR (122 MHz, CD₂Cl₂): δ -20.51 (s, J_{Pt-P} = 2493 Hz). Anal. Calcd for C₂₄H₂₆N₂P₂Pt (599.5): C, 48.03; H, 4.34; N, 4.67%. Found: C, 47.83; H, 4.35; N, 4.45%. IR (cm⁻¹): 2959, ν(CH); 2883, ν(CH); 2215, ν(C≡N); 2109, ν(C≡C).

Synthesis of the CPs. The CPs were synthesized by solvothermal method, whereby L1 was placed in a vial with degassed MeCN under argon. CuX (X = I, Br) was added, and the resulting mixture was stirred for 2 h and heated for 4 h at 80 °C. The solution was slowly cooled to room temperature, and yellow crystals appeared. These were collected and analyzed by single-crystal X-ray diffraction.

Synthesis of CP1, [(Cu₂/₂(L1))_n. L1 (30.0 mg, 0.05 mmol), CuI (19.0 mg, 0.1 mmol), and 5 mL of MeCN. Yield: 63%. Anal. Calcd for C₂₄H₂₆Cu₂I₂N₂P₂Pt (980.38): C, 29.37; H₂, 2.65; N, 2.86%. Found: C, 29.40; H, 2.70; N, 3.20%. IR (cm⁻¹): 2976, ν(CH); 2898, ν(CH); 2231, ν(C≡N); 1981, ν(C≡C).

Synthesis of CP2, [(Cu₂Br₂)(L1))_n. L1 (30.0 mg, 0.05 mmol), CuBr (14.0 mg, 0.1 mmol), and 5 mL of MeCN. Yield: 63%. Anal. Calcd for C₂₄H₂₆Br₂Cu₂N₂P₂Pt (886.4): C, 32.49; H, 2.93; N, 3.16%. Found: C, 33.08; H, 3.21; N, 3.37%. IR (cm⁻¹): 2974, ν(CH); 2913, ν(CH); 2230, ν(C≡N); 1977, ν(C≡C).

Instruments. The ¹H and ¹³P nuclear magnetic resonance (NMR) spectra were recorded on a Bruker Avance 300 Ultrashield NMR spectrometer using CDCl₃ and CH₂Cl₂ as solvents. Elemental analyses were performed on a TruSpec Micro Series for C, H, and N. The infrared (IR) spectra were measured using ABB Bomem, MB series FT-IR spectrometer. Solid-state UV–vis spectra were recorded using Varian Cary 50 spectrophotometer at 298 and 77 K with raised-angle transmittance apparatus having homemade 77 K sample holder. Steady-state fluorescence and excitation spectra were measured on Edinburgh instruments FLS980 phosphorimeter, which is equipped with single monochromators. All samples were crushed prior to use.

The steady-state fluorescence spectra were recorded using capillary. These spectra were corrected for instrument response. Phosphorescence lifetime measurements were made with an Edinburgh instruments FLS980 phosphorimeter equipped with “flash” pulsed lamp. The repetition rate can be adjusted from 1 to 100 Hz. All lifetime values were obtained from deconvolution and distribution lifetime analysis. The latter instrument was also used to measure the chromaticity. The quantum yield measurements were performed with the Horiba Fluorolog III, which is equipped with an integration sphere that allows the direct measurements of emission quantum yields. The thermogravimetric analysis (TGA) traces were acquired on a PerkinElmer TGA 7 apparatus in the temperature range between 20 and 850 °C at 10 °C/min under argon atmosphere. All the figures were treated using the Origin software.

X-ray Crystallography. A clear intense yellow prismatic single crystal of CP1 was measured on a Bruker Kappa APEX II DUO CCD system equipped with a TRIUMPH curved crystal monochromator and a Mo fine-focus tube (λ = 0.710 73 Å). A clear pale yellow prismatic single crystal of L1 and clear intense yellow platelike single crystal of CP2 were measured on a Bruker Apex DUO system equipped with a Cu Kα ImuS microfocus source with MX optics (λ = 1.541 78 Å). Diffraction data were recorded at 173 K for L1, CP1, and CP2. The integration of the data using triclinic, monoclinic, and orthorhombic unit cell yielded total reflections of 3453, 7200, and 32 279 for L1, CP1, and CP2, respectively. The frames were integrated with the Bruker SAINT¹² Software package using a narrow-frame algorithm for CP1 and used wide-frame algorithm for L1 and CP2. Data were corrected for absorption effects using the multiscan method (SADABS).¹² The structures were solved and refined using the Bruker SHELXTL Software Package using space group P1, with Z = 1 for L1, space group P121/m1 with Z = 2 for CP1 and space group Pnma, with Z = 4 for CP2. All non-hydrogen atoms were refined with anisotropic thermal parameters. The hydrogen atoms were placed in calculated positions and included in final refinement in a riding model with isotropic temperature parameters set to U_{iso}(H) = 1.5 U_{eq}(C). Crystal data, data collection, and structure refinement of all compounds are provided in Table S1. The X-ray data for CP2 were of lower quality, despite multiple attempts, due in part to the small size of the crystals available. Both Cu and Mo X-ray sources were also used. When the Mo source was employed, many reflections were overlapping making their integration unreliable. Concurrently, the best data were obtained with the Cu source (R₁ = 0.0925).

Powder X-ray Diffraction. L1, CP1, and CP2 were measured at 173 K on a Bruker APEX DUO X-ray diffractometer. Six correlated runs per sample with Phi Scan of 360° and exposure times of 270 s were collected with the Cu microfocus anode (1.541 84 Å) and the CCD APEX II detector at 150 mm distance. These runs, from -12 to -72° 2θ and from 6 to 36° ω, were then treated and integrated with the XRW2 Eval Bruker software to produce WAXD diffraction patterns from 2.5 to 82° 2θ. The patterns were treated with Diffrac.Eva version 2.0 from Bruker.

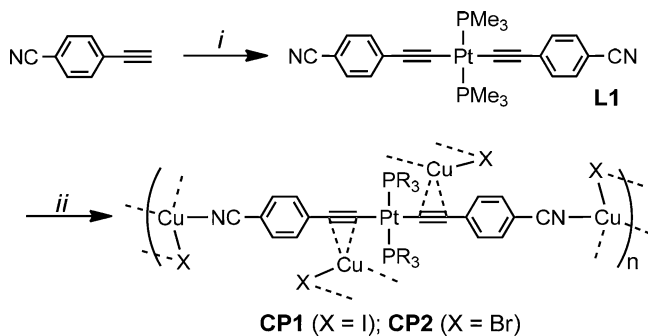
Computations. The calculations done included the density functional theory (DFT) and time-dependent density functional theory (TD-DFT) and were performed with Gaussian 09¹³ at the Université de Sherbrooke with the Mammouth supercomputer supported by Le Réseau Québécois De Calculs Hautes Performances. All cif files from X-ray crystal structures (L1, CP1, CP2) were used for the calculations, except for L1 in solution (for comparison purposes), for which the geometry was optimized. The DFT (singlet and triplet energy states) and TD-DFT calculations^{14–23} were performed using

the B3LYP method. The 6-31g* basis set was used for C, H, N, and P atoms.²³ Valence double ζ (VDZ) with SBKJC effective core potentials were used for all Cu, I, Br, and Pt atoms.^{24–29} The calculated absorption spectra were obtained from GaussSum 3.0.³⁰

RESULTS AND DISCUSSION

Synthesis and Characterization. CP1 and CP2 were prepared by solvothermal reaction using CuX salts (X = I, Br) and L1 in acetonitrile (Scheme 1).

Scheme 1. Synthesis of L1, CP1, and CP2 in MeCN^a



^a(i) *cis*-PtCl₂(PMe₃)₂, NH₄Et₃, CuI. (ii) CuX.

The identity of L1 was confirmed by X-ray crystallography (Figure S1), ¹H and ³¹P NMR (Figures S2–S4), and IR spectroscopy (Figure S5 and Table S2), whereas that for CP1 and CP2 was demonstrated by X-ray structure determination (Figure 1) and IR (Figure S5 and Table S2). The *trans*-geometry of L1 was also confirmed by the value of the coupling constant $J_{\text{Pt-P}} = 2493$ Hz.³¹

The X-ray data for L1 reveal that the CC≡C–Pt–C≡CC axis is quasilinear (average $\angle\text{C–C}\equiv\text{C} \approx 175.1^\circ$ and $\angle\text{Pt–C}\equiv\text{C} \approx 176.5^\circ$). The $\nu(\text{C}\equiv\text{C})$ (2109 cm^{–1} for L1) and $\nu(\text{C}\equiv\text{N})$ (2215 cm^{–1} for L1) modes were also modified upon coordination with the CuX salts (for both CPs, respectively, at ~ 1979 and ~ 2231 cm^{–1}). The decrease of ~ 30 cm^{–1} for $\nu(\text{C}\equiv\text{C})$ is consistent with the expected back-donation from the electron-rich Cu(I) center. The X-ray data for CP1 and CP2 reveals that indeed both coordination sites ($\eta^2\text{-C}\equiv\text{C}$ and C≡N:) are used by the Cu metals forming CP networks (Figure 1). No crystallization solvent molecule was detected in the lattice making these CPs nonporous. This trait resembles that for the 2D CP $[\{\text{Cu}_2(\mu_2\text{-Br})_2(\text{L}2)_2\}_n]^{10b}$ and is explained by the relative orientation of one of the two L2 ligands that places the C₆H₄ planes near parallel to the 2D plane of the CP. This geometry prevents formation of cavities susceptible to host a solvent molecule. Conversely, the $[\{\text{Cu}_4(\mu_2\text{-I})_4(\text{L}2)_2\}_n]$ CP exhibits cavities that can accommodate acetonitrile, propionitrile, or methanol.¹⁰ In this case, all the C₆H₄ planes adopted a relative orientation rather perpendicular to the CP plane, thus forming approximately square cavities. For both CP1 and CP2, L1 exhibits one of the two C₆H₄ planes placed nearly flat with the 2D geometry of the CP layers. This feature also prevents the formation of pores in the lattice.

The key features of CP1 and CP2 are that L1 exhibits major distortions (note that the L1 ligand adopts quasi-identical structures in both cases) and the CPs use $\{\text{Cu}_2(\mu_2\text{-X})_2\}$ SBUs exhibiting both *trans*- (X = I) and *cis*-geometries (X = Br; Figure 2). Noteworthy, the two parameters that differ the most from the most [Pt]-containing CPs are the C–C≡C angles

and the dihedral angles made by the C₆H₄ aromatic planes (see Table 1 (three entries: L1, CP1, and CP2) and the comparative Table S3 containing all related CPs (16 entries for CPs and 4 entries for their corresponding metal–ligands)).^{2,10,32} These tables compare the interplanar C₆H₄⋯C₆H₄ distances, C–C≡C angles, and dihedral angles formed by C₆H₄ planes and the PtP₂C₂ one of related zero-dimensional (0D) complexes and 1D and 2D CPs. The most remarkable feature is the dihedral angles formed by the two C₆H₄ aromatics (90°), which is by far the largest in this series (i.e., 16 CPs and 4 complexes). The only exception is the one for the 1D CP of formula $[(\text{Cu}_2\text{Cl}_2)\text{L}2\text{-PhCN}]_n^{10b}$ which exhibits a similar angle of 86.77°. Similarly, C–C≡C angles averaging 159.7° (CP1) and 158.4° (CP2) are the fourth smallest one when averaging all angles. The three other examples that exhibit C–C≡C angles less than 158.4° are 1D $[(\text{Cu}_2\text{Br}_2)\text{L}3]_n$ (155.0°),^{10a} 1D $[(\text{Cu}_2\text{Cl}_2)\text{L}3]_n$ (155.3°)^{10a} (L3 = MeSC₆H₄C≡C–Pt(PEt₃)₂–C≡CC₆H₄SM_e), and 1D $[(\text{Cu}_2\text{I}_2)(\text{PhCN})\text{L}2]_n$ (156.9°).^{10b} Conversely, these last examples show no distortion in the C₆H₄⋯C₆H₄ dihedral angle (i.e., 0°). In conclusion, L1 appears the most distorted [Pt]-ligand.

The CuX salts (X = Cl, Br, I) are known form various SBUs during the formation of CPs, including the frequently encountered Cu₄I₄L₆ step cubane, Cu₄I₄L₄ cubane, Cu₄I₄L₆ open cubane, and Cu₆I₆L₆ hexagonal prism (L = N-, S-, O-, $\eta^2\text{-C}\equiv\text{C}$). However, the rhomboid Cu₂X₂L₄ (X = Cl, Br, I) is by far the most common motif encountered indicating that this geometry appears to be the most accommodating, presumably because of its small size.³³ Concurrently, this list of possible geometries for SBUs is also far from being exhaustive (Cu₈I₈L₆ fused dicubane,³⁴ (CuXL)_n staircase polymer,³³ Cu₅Br₅L₆ capped square,³⁵ among many others), hence demonstrating the rather high flexibility of these (CuX)_n clusters. In this work, a mixed-ligand environment is present (L = CN, L' = $\eta^2\text{-C}\equiv\text{C}$), and unsurprisingly rhomboid Cu₂X₂L₂L'₂ SBUs are observed. Interestingly both geometries, *trans*- (CP1) and *cis*- (CP2) were isolated. Many precursors of the *trans*-Cu₂X₂L₂L'₂ motifs exist (X = Cl, Br, or I; L and L' = (N-donor/ $\eta^2\text{-C}\equiv\text{C}$),³⁶ (L = C-/P-donor),³⁷ (B- $\eta^2\text{-C}\equiv\text{C}$ /P-donor),³⁸ ($\eta^2\text{-C}\equiv\text{C}$ /P-donor),³⁹ (S-donor/N-donor),⁴⁰ (Se-donor/N-donor),⁴¹ (S-donor/P-donor)⁴²). Conversely, the *cis* form is extremely rare and does not exist, unless a bridging ligand forces this type of geometry.^{11,43} In CP2, the *cis* geometry is obtained without the use of a bridging ligand. To the best of our knowledge, this feature is unique. Instead, a large chelating frame composed of two $\leftarrow\text{N}\equiv\text{C}-\text{C}_6\text{H}_4-\text{C}\equiv\text{C}$ branches (from two different L1 ligands) and one central rhomboid ($\eta^2\text{-C}\equiv\text{C}$)₂Cu₂Br₂ SBU play together the role of this pseudobridging assembly and bind two Cu atoms of the rhomboid on the same face through Cu–N links. The resulting structure of the *cis*-rhomboid is not planar but rather exhibits a butterfly geometry, which has also been observed for the other rare examples.⁴³ This distortion from planarity is also consistent with the rather high degree of flexibility of the (CuX)_n SBUs (X = Cl, Br, I; n = 2–8).

Thermal Stability and X-ray Powder Diffraction Patterns. The thermal stability of L1, CP1, and CP2 was evaluated by TGA (Table 2, Figure 3). The first weight losses are noted at ~ 260 , ~ 261 , and ~ 271 °C with mass loss of 3, 3, and 19% for L1, CP1, and CP2 corresponding to the decomposition of the ligand via the loss of C≡N (theory = 4%), C≡N (3%), and $[2(\text{C}\equiv\text{N}) + (\text{C}_8\text{H}_4)]$ (17%), respectively. This thermal stability ($T_{\text{dec}} > 240$ °C) is considered good for a CP. The second weight losses show a

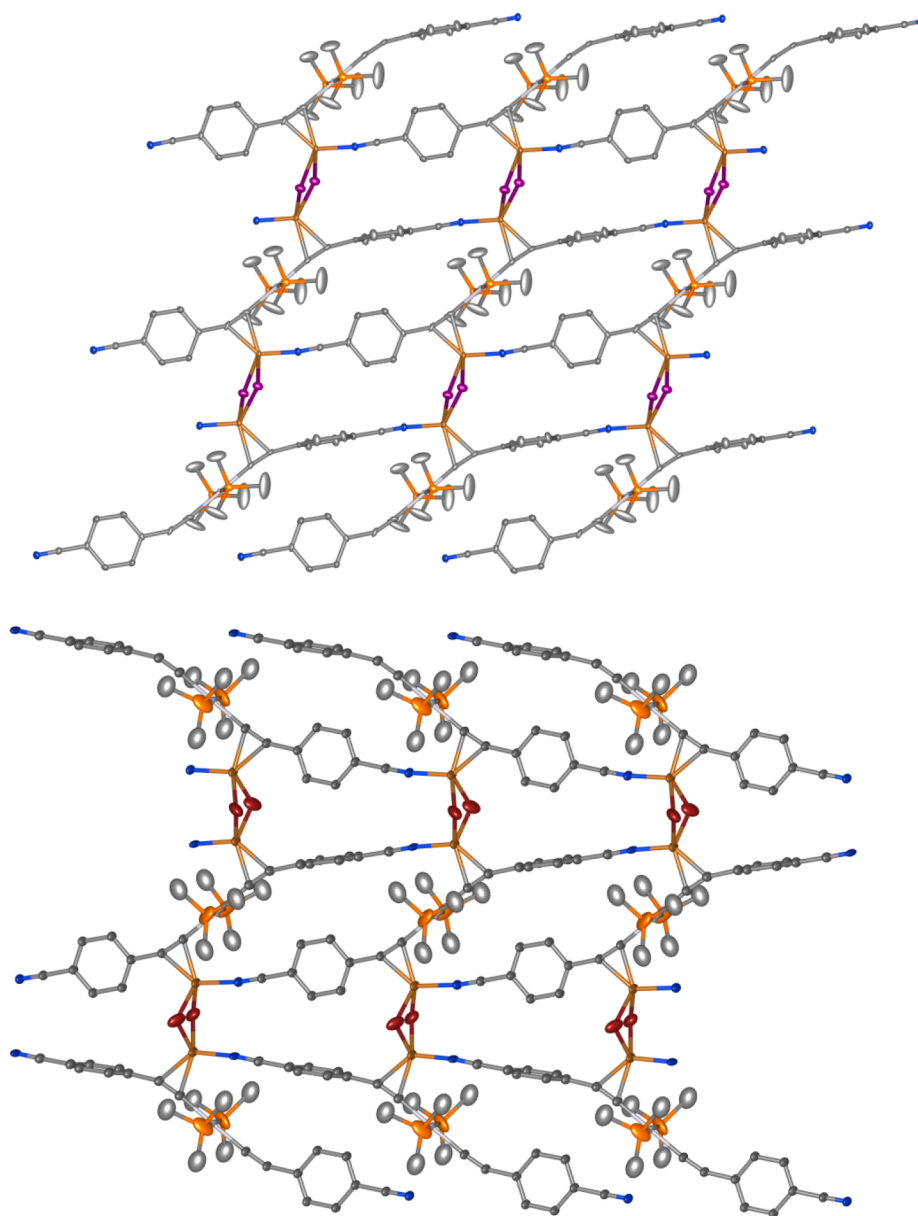


Figure 1. Crystal structures of the 2D polymers **CP1** (top) and **CP2** (bottom): Cu = gold, Br = brown, I = purple, Pt = pale gray, P = orange, C = gray, and N = blue. The thermal ellipsoids are represented at 50% probability, respectively. The H atoms are omitted for clarity.

very similar pattern at a plateau starting at ~ 375 , 355 , and ~ 405 °C with weight loss of 32, 21, and 11% for **L1**, **CP1**, and **CP2**, respectively. These weight losses correspond to the loss of two (C_8H_4) (theory = 33), two (C_8H_4)₂ (20), and one (C_8H_4) (11%) for **L1**, **CP1**, and **CP2**, respectively. The third weight loss of 25 (26) and 12 (theory = 9%) at ~ 570 and ~ 510 °C correspond to the loss of I_2 and (PMe_3) for **CP1** and **CP2**, respectively. The residual masses at temperature greater than 850 °C are 65 (theory = 63), 51 (51), and 58 (61%) for **L1**, **CP1**, and **CP2**, respectively.

For the purpose of the photophysical measurements, the powdery samples were analyzed by powder X-ray diffraction (PXRD; Figure 3). The experimental traces matched well the calculated ones based on the single-crystal data. No other phase (crystalline nor amorphous, generally depicted by a large halo) was detected.

Photophysical Characterization of L1. **L1** was first examined in both solution and solid state at 298 and 77 K for

comparison purposes with its CPs (Figure 4). **L1** exhibits a fluorescence and phosphorescence band, respectively, in the 350–450 and 450–700 nm windows (the peak positions are indicated in Figure 4 or the figure caption). These assignments are based on the time scale of their respective lifetimes (i.e. <90 ps and μs , respectively; see details below), their Stokes shifts (1900–2400 and 6300–9800 cm^{-1} , respectively), literature precedents on this well-known type of chromophore,⁴⁴ and the DFT computations below. Because **L1** is found much distorted within the 2D layer of **CP1** and **CP2**, an optimized geometry of **L1** was computed for comparison purposes but also to correlate its properties in solution.

For characterization purposes, the optimized geometries of **L1** in the ground (S_0) and lowest triplet excited states (T_1) to define its properties in solution are presented in Figure 5. The computed dihedral angles made by the C_6H_4 aromatics and the PtP_2C_2 planes are 90° and 0° , respectively, for the S_0 and T_1 states. Both geometries agree with previous DFT investigations

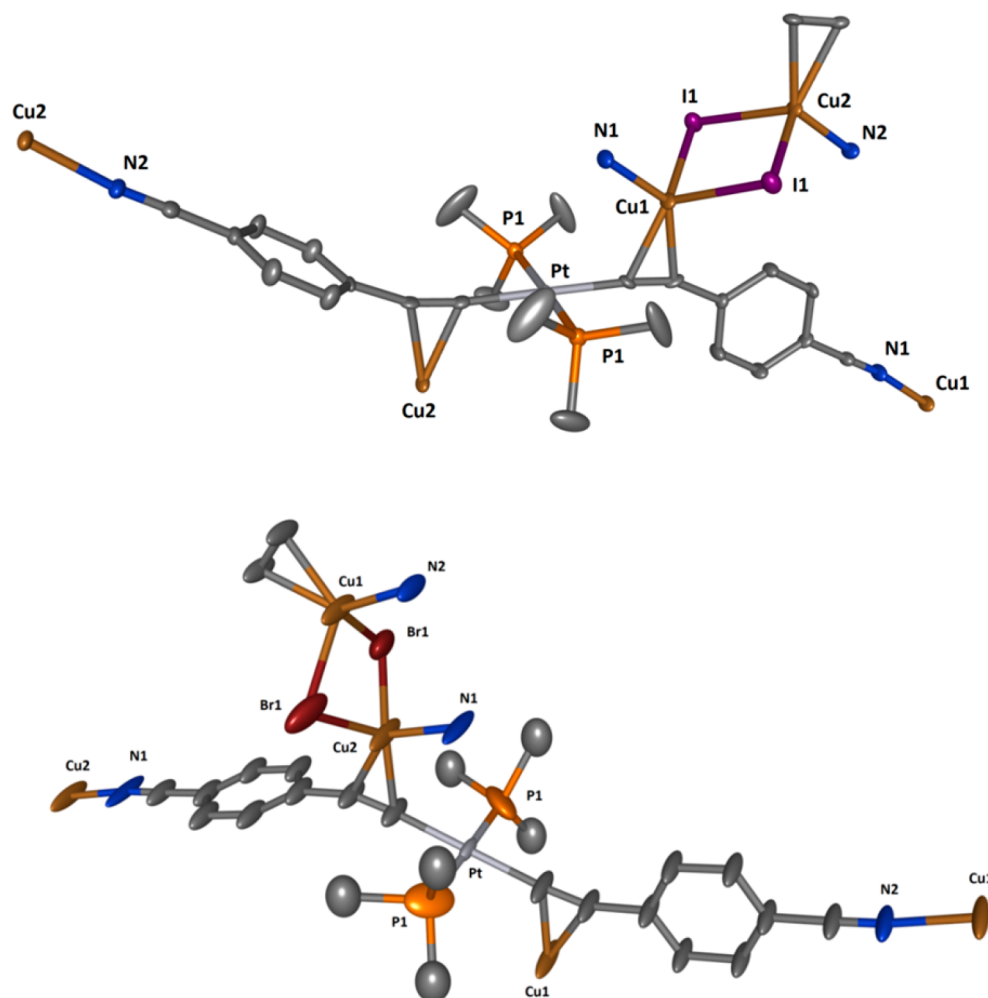


Figure 2. X-ray structure of L1 within the CP1 and CP2 lattice. (top) View of a segment of the 2D CP1. The H atoms are hidden for clarity. Selected bond lengths (Å) and angles (deg): Cu1...Cu2 3.5786(4), Cu1–I1 2.7497(4), Cu2–I1 2.7074(4), Cu2–N2 1.981(4), Cu1–N1 1.974(4), I1...I1 4.1136(4); Cu2–I1–Cu1 81.954(15), N2–Cu2–I1 105.43(7), I1–Cu2–I1#7 98.88(2), N2–Cu2–I1#7 105.43(7). Symmetry transformations used to generate equivalent atoms: #7 $x, -y + 1/2, z$. (bottom) View of a segment of the 2D CP2. The H atoms are hidden for clarity. Selected bond lengths (Å) and angles (deg): Cu1...Cu2 3.191(6), Cu1–Br1 2.544(4), Cu2–Br1 2.577(4), Cu1–N2 1.949(19), Cu2–N1 2.003(17), Br1...Br1 3.899(6); Cu1–Br1–Cu2 77.08(13), N2#6–Cu1–Br1 101.9(3), Br1–Cu2–Br1#7 98.26(16), Br1#7–Cu1–Br1 100.00(16), N1#2–Cu2–Br1#7 103.2(3). Symmetry transformations used to generate equivalent atoms: #6 $x + 1/2, -y + 1/2, -z + 5/2$; #7 $x, -y + 1/2, z$.

Table 1. Interplanar $C_6H_4 \cdots C_6H_4$ Distances (d), $C-C \equiv C$ Angles, and Measured Angles between Planes A, B, and C^a

dihedral angle					dimension-CP
$\angle C-C \equiv C^a$ (deg)	$\angle Pt-C \equiv C^a$ (deg)	A/B (deg)	B/C (deg)	A/C (deg)	
175.2 (1.9)	175.0 (2.0)	38.7	33.9	4.8	0D-LI($X' = CN$; R = Me)
175.0 (2.0)	178.0 (1.6)				
157.7 (4)	174.2 (4)	90	31.0	90	2D- $[(Cu_2I_2)_2L1]_n$ (CP1)
161.8 (4)	172.7 (4)				
159 (2)	174 (2)	90	31.4	90	2D- $[(Cu_2Br_2)_2L1]_n$ (CP2)
158 (2)	174 (2)				

^aThe esd values are in parentheses.

on other related complexes in their S_0 ⁴⁵ and T_1 ⁴⁶ states. This computational outcome corroborates the recently reported very low-energy barrier to rotation around the Pt–C bonds,⁴⁷ which is also well-perceived in Tables 1 and S3. The bond angles $\angle C-C \equiv C$ and $\angle Pt-C \equiv C$ are rather linear for the uncoordinated ligand L1.

The molecular orbital (MO) representations for the highest-occupied molecular orbital (HOMO) and lowest-unoccupied molecular orbital (LUMO) for S_0 analysis and lowest-semioccupied (LSOMO) and highest-semioccupied molecular orbitals (HSOMO) for T_1 study are presented in Figure 5. The relative atomic contributions distributed over various molecular fragments ($C \equiv C$, C_6H_4CN , $Pt(PMe_3)_2$) for the frontier MOs are provided in Tables 3 and 4 for the S_0 and T_1 states, respectively. Qualitatively, these computational results for both the optimized geometry of L1 and its X-ray structure indicate that the nature of both excited states (S_1 : ${}^1(\text{HOMO})^1(\text{LUMO})$, T_1 : ${}^1(\text{LSOMO})^1(\text{HSOMO})$) are intraligand $\pi\pi^*$ ($CNC_6H_4C \equiv C$) mixed with metal-to-ligand charge transfer (MLCT), which is consistent with the previous conclusions.^{45,46} This compar-

Table 2. TGA Data for L1, CP1, and CP2^a

	T (°C), Δ_{mass} ; exp (calc%)	T (°C), Δ_{mass} ; exp (calc%)	T (°C), Δ_{mass} ; exp (calc%)	T (°C), Δ_{mass} ; exp (calc%)
L1	~260, 3 (4) [C≡N]	~375, 32 (33) [(C ₈ H ₄) ₂]		>850, 65 (63)
CP1	~261, 3 (3) [C≡N]	~355, 21 (20) [(C ₈ H ₄) ₂]	~570, 25 (26) [I ₂]	>850, 51 (51)
CP2	~271, 19 (17) [(C≡N) ₂ + (C ₈ H ₄) ₂]	~405, 11 (11) [(C ₈ H ₄) ₂]	~510, 12 (9) [PMe ₃]	>850, 58 (63)

^aThe proposed fragment losses are placed inside the brackets.

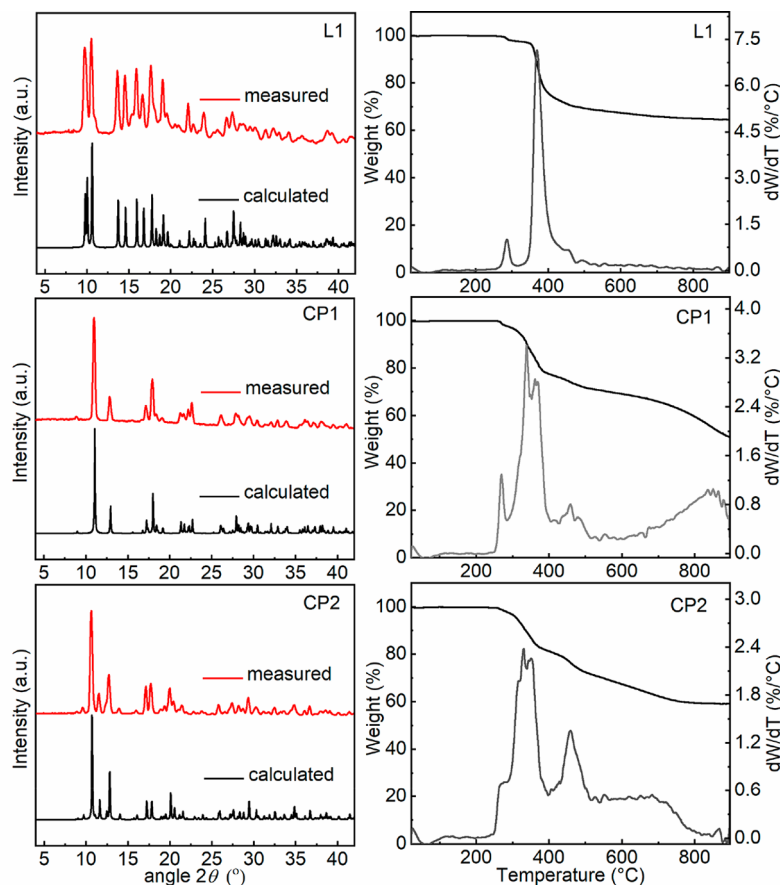


Figure 3. (left) Comparison of the experimental (red) and calculated (black) PXRD patterns for L1, CP1, and CP2. (right) TGA traces (black) and its 1st derivative (gray) for L1, CP1, and CP2.

ison suggests that the nature of the excited states of L1 is influenced slightly by minor structural distortions.

Moreover, TD-DFT computations (Table 5) place the S_0 – S_1 electronic transitions at ~343 and ~373 nm, respectively, for L1 (in its optimized geometry using a THF solvent field) and in the crystal lattice (no geometry optimization is applied). These values compare well to the absorption features in solution and in the solid state ($\lambda_{\text{max}} \approx 350$ nm; Figure 4).

Similarly, the position of the phosphorescence of L1 was predicted by DFT by calculating the energy difference between the total energy of L1 in the S_0 and T_1 states (Table 6). The position of the $T_1 \rightarrow S_0$ electronic transition calculated for L1 in 2MeTHF is 499 nm (using the optimized geometries), which compares reasonably with the experimental positions of 473 nm. However, the calculated one for L1 in the solid state is 445 nm (using strictly the X-ray data) and does not match that in the solid state (522 nm). The main reason is that this calculation does not take into account the true structure in the triplet state, as geometry optimization (here in the T_1 state) is simply not possible in the solid state for obvious steric reasons. The true geometry within the constraint of a crystal lattice is

obviously unknown. To overcome this problem, a correction factor is applied defined as the difference in calculated (445 nm) and experimental (522 nm) positions of the maximum (3346 cm^{-1}).

The phosphorescence maxima and lifetimes τ_p values for L1 in the solid state are placed in Table 7. Expectedly, the peak maxima compare to those for L2,^{10b} and in both cases, biexponential kinetics are depicted (as well as in glassy matrices at 77 K; see the τ_p data in the caption of Figure 4). The reason for this complexity was recently outlined in detail.⁴⁸ In short, the [Pt] motif exhibits a high degree of rotational flexibility around the Pt–CC bonds and often the presence of different dihedral angles (as listed in Table 1 and Table S3); different site in the lattice (more than one molecule per unit cell or placed at the surface of the crystal) leads to different specific τ_p values. In glassy matrices (i.e., 77 K), computations demonstrated that, in fact, multiple trapped stable conformations exist, again each exhibiting their own τ_p values. The reason stems from the shape of the Pt d orbitals that could accommodate the sp-hybridized C≡C groups. In brief, in these experimental conditions, multiple exponential emission decays

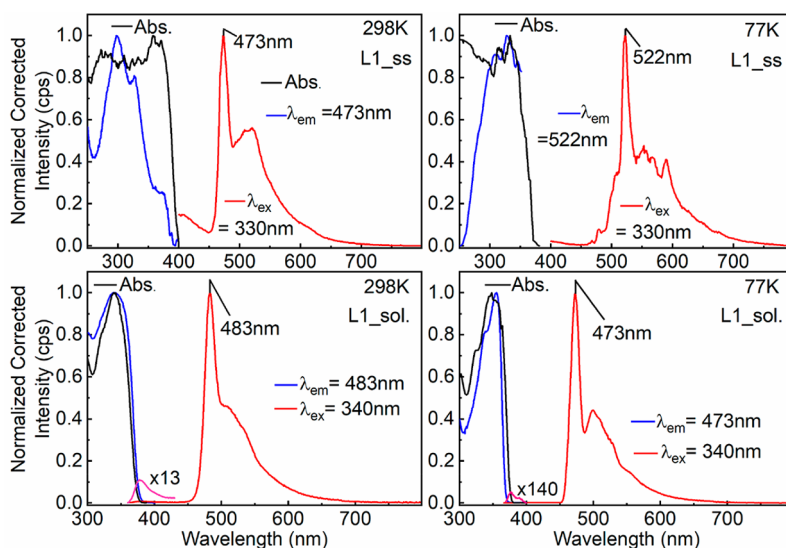


Figure 4. Emission (red), excitation (blue), and absorption (black) spectra of **L1** in solid state [ss] (top) and in 2MeTHF [sol] (bottom) at 298 K (left) and 77 K (right). The lifetime τ_p of **L1** in 2MeTHF at 77 K is 70.3 μ s (B_1 : 0.0551; f_1 : 60%) and 120 μ s (B_2 : 0.0221; f_2 : 40%; $f_i(\%) = (B_i\tau_i) / \sum(B_i\tau_i) \times 100$; $I_p(t) = B_1 \exp(-t/\tau_1) + B_2 \exp(-t/\tau_2) + B_3 \exp(-t/\tau_3) + \dots$; $\chi^2 = 1.027$), and at 298 K, it is 0.77 μ s (f_1 : 99.73%; $\chi^2 = 1.088$). The presence of a double exponential is explained below. The fluorescence lifetimes τ_F are below the IRF of the instrument (i.e., <90 ps). The emission spectra for solid samples are limited by glassware (cutoff at 400 nm). The position of the weak fluorescence signals (λ_F) are as follow: \sim 400, 374, and 375 nm for **L1** in the solid state at 298 K and in solution at 298 and 77 K, respectively.

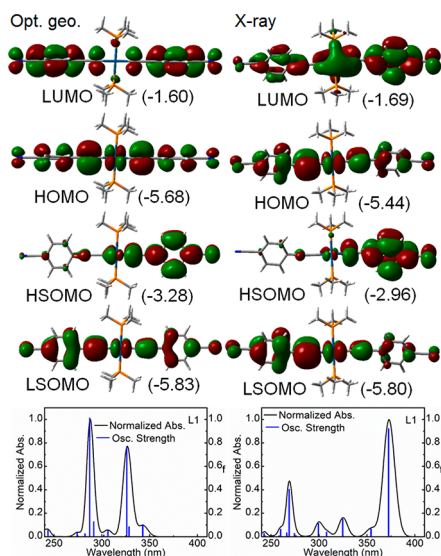


Figure 5. (upper) Representations of the HOMO, LUMO, LSOMO, and HSOMO of **L1** (optimized geometry (left) and X-ray structure (right)); energies in eV; see Figures S6 and S7 for more MOs). (lower) Bar graph reporting the calculated oscillator strength (f) and calculated positions (by TD-DFT) of the first 100 electronic transitions for **L1** from its optimized geometry using a THF solvent field (left) and X-ray structure. The black line is generated by assigning an arbitrary fwhm of 1000 cm^{-1} to each transition.

(generally two or three) are to be expected. In fluid solution at room temperature, the decay is monoexponential ($\tau_p = 0.77 \mu$ s; $\pm 5\%$), which is consistent with the low energy of rotation around the Pt–CC bond.

Photophysical Properties of CP1 and CP2. The absorption, excitation, and emission spectra of **CP1** and **CP2** are shown in Figure 6, and the emission data are summarized in Table 7.

Table 3. Relative Atomic Contributions (%) of the Various Fragments to the Frontier MOs of L1 in Its Optimized Geometry and the X-ray Structure^a

opt geo	H-2	H-1	HOMO	LUMO	L+1	L+2
2(C \equiv C)	36.9	47.7	41.1	11.0	8.6	13.0
2(C ₆ H ₄ CN)	37.4	13.8	34.3	81.4	85.8	9.7
Pt(PMe ₃) ₂	25.7	38.5	24.6	7.6	5.5	77.3
X-ray	H-2	H-1	HOMO	LUMO	L+1	L+2
2(C \equiv C)	35.1	54.6	43.4	10.7	12.0	1.0
2(C ₆ H ₄ CN)	52.0	12.7	30.0	72.3	73.7	90.4
Pt(PMe ₃) ₂	12.8	32.7	26.7	16.9	14.3	8.5

^aH = HOMO, L = LUMO; the values in bold represent contributions greater than 35%. See Tables S4 and S5 for more MOs.

From a comparison with other related CPs containing the [Pt]-type ligands, **CP1** and **CP2** at 298 K exhibit the largest emission quantum yields Φ_p ($\sim 30\%$) and the most red-shifted peak maxima (640 and 650 nm) of the whole series (Table S8). Moreover, these CPs exhibit particularly broad emission bands (i.e., full width at half-maximum (fwhm) ranging from 3000 to 5000 cm^{-1}). Conversely, their emission lifetime values τ_p compare relatively favorably with these related species. The emission time scale (μ s) and particularly large Stokes shifts (11 900–13 400 cm^{-1}) indicate the presence of triplet emissions. Biexponential emission decays are also observed, but due to the unavoidable presence of different sites of occupations in the solids (e.g., core and surface sites) as previously well-demonstrated for other related [Pt]-compounds.⁴⁸

DFT and TD-DFT Calculations. Fragments of the X-ray structures were used as models (i.e., input files) for DFT and TD-DFT computations to provide information on the nature of the S_1 and emissive T_1 excited states for **CP1** and **CP2**.

The visual representations of the frontier MOs (HOMO and LUMO for singlet; LSOMO and HSOMO for triplet) for **CP1** and **CP2** are shown in Figure 7, and the relative atomic

Table 4. Relative Atomic Contributions (%) of the Various Fragments to the Semi-Occupied MOs of L1^a in Its Lowest-Energy Triplet Excited State^b

fragments	optimized geometry				X-ray structure			
	LS-1	LSOMO	HSOMO	HS+1	LS-1	LSOMO	HSOMO	HS+1
2(C≡C)	55.3	35.8	16.3	10.4	54.9	44.1	10.4	14.5
2(C ₆ H ₄ CN)	12.8	41.1	75.7	80.1	12.0	30.5	83.3	61.1
Pt(PMe ₃) ₂	31.8	23.1	8.0	9.5	33.1	25.3	6.3	24.5

^aOptimized a with THF solvent field. ^bHS = HSOMO, LS = LSOMO; the values in bold represent contributions greater than 40%.

Table 5. Calculated Positions, Oscillator Strengths (*f*), and Major Contributions of the First Five Singlet–Singlet Electronic Transitions for L1^a

opt geo	λ (nm)	<i>f</i>	major contributions (%)
1	342.8	0.103	H-1→L (73), H→L (19)
2	328.5	0.085	H-1→L+1 (63), H→L (12), H→L+1 (11)
3	326.1	0.763	H-1→L (13), H-1→L+1 (12), H→L (60)
4	306.4	0.054	H-2→L (12), H-1→L+1 (11), H→L+1 (51), H→L+2 (20)
5	302.1	0.015	H→L+1 (12), H→L+2 (69)
X-ray	λ (nm)	<i>f</i>	major contributions (%)
1	372.6	0.922	H→L (91)
2	354.3	0.067	H-1→L (74), H-1→L+1 (18)
3	324.7	0.150	H-2→L (13), H-1→L+1 (12), H→L+1 (64)
4	307.9	0.040	H-1→L (12), H-1→L+1 (57), H→L+1 (17)
5	299.4	0.113	H-2→LUMO (67), HOMO→L+1 (11)

^aOptimized geometry and X-ray structure. See Tables S6 and S7 for the first 100 electronic transitions.

Table 6. Calculated T₁–S₀ Energy Gaps and Calculated Positions (λ_{max}) of the T₁ Emissions for L1,^a CP1, and CP2

compound	T ₁ –S ₀ gap (eV, cm ⁻¹)	calcd	exp	T ₁ –S ₀ gap ^b –3346 cm ⁻¹	corr
		λ _{max} T ₁ →S ₀ (nm)	λ _{max} (77 K; nm)		calcd λ _{max} T ₁ →S ₀ (nm)
L1 opt geo	2.48, 20 003	499	473		
L1 X-ray	2.79, 22 503	445	522	19 157	522
CP1 X-ray	2.73, 21 978	455	590	18 632	537
CP2 X-ray	2.67, 21 505	465	584	18 159	551

^aOptimized geometry using a THF solvent field and X-ray data. ^bA correction factor was applied due to the impossibility to optimize the geometry in the solid state. This factor is based on the well-defined emission of L1 (using X-ray data) as calculated T₁–S₀ gap – experimental T₁–S₀ gap of L1: 22 503 – 19 157 = 3346 cm⁻¹.

contributions of the various fragments building these models to the frontier MOs are placed in Table 8. By examining the low-energy electronic transitions (see, e.g., Table 9), one can monitor the change in atomic contributions in the excited

states. The main conclusion of these computations is that the low-energy spin-allowed electronic transitions generate low-lying metal/halide-to-ligand charge transfer (¹M/XLCT*) excited states. Concurrently, the T₁ excited states (built upon the LSOMO and HSOMO) are also best described by ³M/XLCT*. Similarly, TD-DFT computations place the lowest-energy electronic transitions in the vicinity of 500 nm with weak *f* values (Table 9), precisely where the absorption band starts (see black lines in Figure 6).

In addition, by tracing the calculated oscillator strengths for the first 80 singlet–singlet electronic transitions as a function of their calculated positions, simulated spectra can be generated (Figure 8). Most of these 80 components are located between 350 and 450 nm, which means that, by considering their vibronic progressions, this spectral segment is predicted to be filled with unresolved components. This is precisely what is depicted in Figure 6, where the absorption envelope is essentially broad and unresolved in this 350–450 nm region.

Noteworthy, the calculations of the positions of the S₀ → T₁ electronic transitions using the X-ray data of CP1 and CP2 matrices are, respectively, 455 and 465 nm (Table 6). These calculated positions need to be corrected for the fact that no geometry optimization was applied. This correction factor (3346 cm⁻¹) was deduced using L1 (see above) and is applied

Table 7. Comparison of the Phosphorescence Positions and τ_p Data for L1, CP1, and CP2

	298 K				77 K				
	λ _{max} (nm)	B _i ^a	τ _p ^b (μs)	χ ²	Φ _e ^c (%)	λ _{max} (nm)	B _i ^a	τ _p ^b (μs)	χ ²
0D-L1 ^{tw} (2MeTHF solution)	483		0.77	1.088		473	0.0551 0.0221	70.3 120	1.027
0D-L1 ^{tw} (solid state)	473	0.0876 0.1342	0.46 1.87	1.156	26	522	0.0071 0.0393	32.5 75.0	1.066
2D-[(Cu ₂ I ₂) ₂ L1] _n (CP1) ^{tw}	650	0.0690 0.0092	0.64 7.10	1.052	32	590	0.0292 0.0013	30.4 67.2	1.049
2D-[(Cu ₂ Br ₂) ₂ L1] _n (CP2) ^{tw}	640	0.0156 0.0081	4.27 10.6	1.034	28	584	0.0062 0.0084	15.0 51.0	1.019

^aI_p(*t*) = B₁ exp(–*t*/τ₁) + B₂ exp(–*t*/τ₂) + B₃ exp(–*t*/τ₃) + ... ^bThe uncertainties are ±5%. ^cThe uncertainties are ±10% based on multiple measurements.

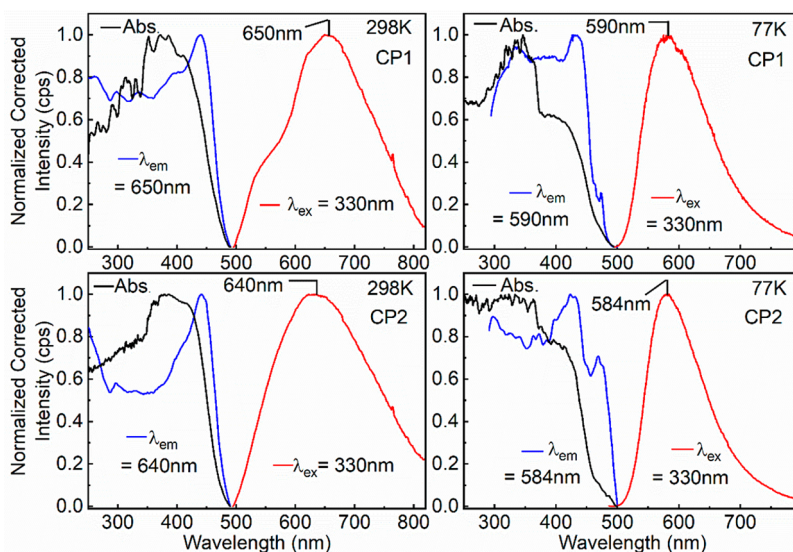


Figure 6. Emission (red), excitation (blue), and absorption (reflectance; black) spectra of CP1 (top) and CP2 (bottom) in solid state at 298 (left) and 77 K (right). The absorption features spreading up to 500 nm in CP1 and CP2 are $S_0 \rightarrow S_1$ absorptions based on TD-DFT computations below.

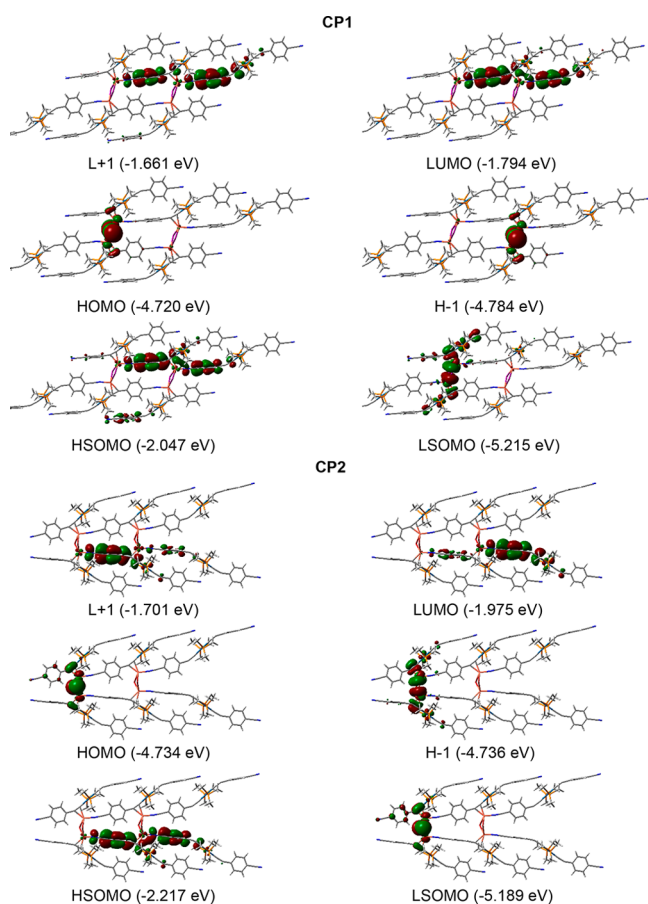


Figure 7. Representations of the frontier MOs for CP1 (top) and CP2 (bottom). See Figures S8 and S9 for more MOs.

for CP1 and CP2 (Table 6). After correction, the predicted positions of the $T_1 \rightarrow S_0$ transitions are, respectively, 537 and 551 nm for CP1 and CP2. These values fall perfectly within the range where the phosphorescence bands appear (i.e., starting at 500 nm, then exhibiting maxima at 590 and 584 nm at 77 K and

at 650 and 640 nm at 298 K) and spread toward the near-IR (Figure 6).

The S_1-T_1 Energy Gaps. DFT (Table 9; $S_0 \rightarrow S_1$, 510 and 504 nm) and TD-DFT (Table 6; $S_0 \rightarrow T_1$, 537 and 551 nm) clearly predict a very small S_1-T_1 energy gap. Experimentally, time-resolved spectroscopy shows no evidence for the existence of other short-lived components (here sought in the picosecond time scale (i.e., ≤ 90 ps) for this type of metalloligand), indicating that no fluorescence is detected. This observation is fully consistent with the heavy atom effect associated with the presence of Cu_2X_2 rhomboids ($X = Br, I$) directly coordinated onto L1. These two observations combined are also corroborated by examining the unresolved (0–0) origins of both the absorption band on the low-energy side and the phosphorescence on the high-energy side. Indeed, both origins appear in the vicinity of 500 nm with no or almost no spectral overlap between the two (Figure 6). This is also consistent with the large Stokes shifts ($11\,900-13\,400\text{ cm}^{-1}$). Concurrently, L1 in 2MeTHF exhibits a well-defined fluorescence band at 375 nm, and this overlaps clearly with the absorption (Figure 4). All these observations and comparisons indicate that indeed the S_1-T_1 energy gaps must be small.

Usually, small S_1-T_1 energy gaps are associated with perpendicularly oriented singlet- and triplet-state manifolds, where the two unpaired electrons are located (like in $n\pi^*$ states). The representations of the frontier MOs illustrate well with this orientation situation (Figure 7) and bear their importance for the interpretation of the excited-state properties of these novel CPs. In conclusion, all of these computations and comparisons support the $^1,^3M/XLCT^*$ assignments, which are unsurprisingly essentially the same as that was made for the other related CPs listed in Table S8.^{10b} However, these computational predictions and experimental observations of a small S_1-T_1 energy gaps are new.

Structure–Property Relationship. Both CP1 and CP2 exhibit the most red-shifted triplet emissions among all the CPs using the *trans*-Pt(PMe₃)₂(C≡CC₆H₄X)₂ metalloligands. These new CPs are built upon Cu- η^2 -C≡C and Cu-X coordinations ($X = CN, SMe$), and L1 undergoes stress from both fragments simultaneously, inducing distortions along the

Table 8. Relative Atomic Contributions of the Various Fragments to the CP Frontier MOs^a

	singlet (in %)				triplet (in %)			
	H - 1	HOMO	LUMO	L + 1	LS - 1	LSOMO	HSOMO	HS + 1
CP1								
L1	6.8	6.8	91.4	96.9	9.0	36.1	88.3	97.1
Cu	31.3	31.4	7.8	2.8	30.3	34.2	10.7	2.4
I	61.9	61.7	0.8	0.3	60.7	29.7	1.0	0.4
CP2								
L1	24.6	11.0	97.3	94.9	31.0	13.6	94.0	97.8
Cu	44.4	41.9	2.2	4.5	37.9	38.3	5.0	2.0
Br	31.0	47.1	0.5	0.5	31.1	48.1	1.0	0.2

^aMajor contributions in bold. See Supporting Information for more MOs in the singlet state. See Tables S9 and S10 for more MOs.

Table 9. Calculated Positions, Oscillator Strength (f), and Major Contributions of the First Two Singlet–Singlet Electronic Transitions for CP1 and CP2^a

λ (nm)	f	major contributions (%)
CP1		
510.0	0.0007	HOMO–1→LUMO (85)
502.2	0.0004	HOMO→LUMO (71), HOMO→LUMO+1 (18)
CP2		
503.7	0.0005	HOMO→LUMO (39), HOMO→LUMO+1 (58)
502.2	0.0364	HOMO–1→LUMO (42), HOMO–1→LUMO+1 (55)

^aSee Tables S11 and S12 for the first 80 electronic transitions.

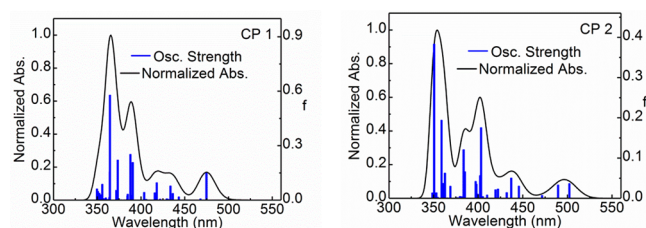


Figure 8. Bar graph reporting the calculated oscillator strength and calculated position of the first 80 electronic transitions calculated by TD-DFT for CP1 and CP2 (bar graph; f = computed oscillator strength). The black line is generated by assigning an fwhm = 1000 cm^{-1} to the transition.

$\angle(\text{C}-\text{C}\equiv\text{C})$ bond angles and dihedral angles (θ_{da}) made by the planes A, B, and C (Table 1). The optimized geometry of L1 (in the gas phase) in its triplet state exhibits all three dihedral angles $\theta_{\text{da}} = 0^\circ$ (see above). Consequently, deviations from this value represent a distortion. The most relevant way to quantify this distortion for comparison purposes is to add all three ($\sum\theta_{\text{da}}$). By comparing the phosphorescence maxima with $\angle(\text{C}-\text{C}\equiv\text{C})$ bond angles and $\sum\theta_{\text{da}}$ (Table 10), a clear correlation is depicted. In brief, more distorted L1 is, more red-shifted the $^3(\text{M}/\text{XLCT})^*$ emission is.

Table 10. Comparison of the Emission Maxima with Structural Parameters of the 2D-CPs

2D-CP	ref ^a	λ_{max} (nm) 298, 77 K	av $\angle(\text{C}-\text{C}\equiv\text{C})$ (deg) ^b	av $\angle(\text{Pt}-\text{C}\equiv\text{C})$ (deg) ^b	$\sum\theta_{\text{da}}$ (deg) ^c
$[(\text{Cu}_2\text{I}_2)_2\text{L1}]_n$ (CP1)	tw	650, 590	159.8	173.5	211
$[(\text{Cu}_2\text{Br}_2)_2\text{L1}]_n$ (CP2)	tw	640, 584	158.5	174	211
$[(\text{Cu}_2\text{Br}_2)_2\text{L2}]_n$	10b	603, 575	161.0	173.6	80
$[(\text{Cu}_2\text{Br}_2)_2\text{L2}]_n$	10b	586, 571	162.0	173.9	63
$[(\text{Cu}_4\text{I}_4)_2\text{L2-PrCN}]_n$	10b	568, 555	163.3	175.5	72

^atw = this work. ^bAverage (av) angles from Table 1 or ref 10b. ^cSums of the dihedral angles from Table 1 or ref 10b. Note that the esd values are placed with the data in Table 1 or ref 10b.

CONCLUSION

This work demonstrated that this new organometallic ligand L1, belonging to a family of complexes often presented as rigid sticks, can be significantly distorted by rather soft and usually readily adaptable $(\text{CuX})_2$ SBUs ($X = \text{halide}$, here Br and I; $n = 1, 2, 3, \dots$). This adaptability was demonstrated by the presence of two geometries for the SBUs formed: *trans*- Cu_2I_2 (common) and *cis*- Cu_2Br_2 (extremely rare). These distortions for L1 turn out to be the largest ever observed for this category of complexes (denoted [Pt]), and yet, the TGA traces indicated a rather good thermal stability ($T_{\text{dec}} > 250^\circ\text{C}$). The two new CPs are also very luminescent ($\Phi_e \approx 30\%$) and exhibit the most red-shifted maxima (650 nm) at 298 K. The lowest-energy excited states are $^1^3\text{M}/\text{XLCT}^*$ based upon DFT and TD-DFT computations and comparisons of experimental findings, but very interestingly, the S_1-T_1 energy gaps are predicted to be unusually small. The main conclusion is that the presence of $\text{Cu}(\eta^2-\text{C}\equiv\text{C})$ binding in the [Pt] ligands, which is more favored over the $\text{Cu}-\text{S}$ link,^{10a,b} distorts its scaffolding in various extents as illustrated in Table 1 (and Table S3). This feature means that the preparation of porous materials, including metal–organic frameworks, is impeded by this $\text{Cu}(\eta^2-\text{C}\equiv\text{C})$ trait. To avoid such distortions and the undesired $\text{Cu}(\eta^2-\text{C}\equiv\text{C})$ interactions, steric constraints about the Pt(II) atom must be considered in future designs.

■ ASSOCIATED CONTENT

● Supporting Information

The Supporting Information is available free of charge on the ACS Publications website at DOI: 10.1021/acs.inorgchem.8b00899.

X-ray data, IR, ^1H and NMR ^{31}P spectra, representations of the frontier MOs, relative atomic contributions of the various fragments to the frontier MOs, calculated positions, oscillator strengths, and major contributions of the first 100 or 80 singlet–singlet electronic transitions of **L1**, **CP1**, and **CP2**, comparison of the interplanar $\text{C}_6\text{H}_4\cdots\text{C}_6\text{H}_4$ distances, $\text{C}-\text{C}\equiv\text{C}$ angles and measured angles between planes A, B, and C, comparison of the emission positions and τ_{p} data for **L1**, **CP1**, and **CP2** with related materials (PDF)

■ Accession Codes

CCDC 1834540–1834542 contain the supplementary crystallographic data for this paper. These data can be obtained free of charge via www.ccdc.cam.ac.uk/data_request/cif, or by emailing data_request@ccdc.cam.ac.uk, or by contacting The Cambridge Crystallographic Data Centre, 12 Union Road, Cambridge CB2 1EZ, UK; fax: +44 1223 336033.

■ AUTHOR INFORMATION

■ Corresponding Author

*E-mail: Pierre.Harvey@USherbrooke.ca.

■ ORCID

Daniel Fortin: 0000-0002-0223-6362

Pierre D. Harvey: 0000-0002-6809-1629

■ Notes

The authors declare no competing financial interest.

■ ACKNOWLEDGMENTS

This work was supported by the Natural Sciences and Engineering Research Council of Canada, the Fonds de recherche du Québec-Nature et technologies, Compute Canada and Calcul Québec, and the Centre Québécois sur les Matériaux Fonctionnels.

■ REFERENCES

- (1) (a) Crabtree, R. H. The stability of organometallic ligands in oxidation catalysis. *J. Organomet. Chem.* **2014**, *751*, 174–180. (b) Sobota, P.; John, L. Organometallic Compounds in the Synthesis of New Materials: Old Ligands, New Tricks. In *Advances in Organometallic Chemistry and Catalysis: The Silver/Gold Jubilee International Conference on Organometallic Chemistry* Celebratory Book; John Wiley & Sons, Inc., 2013; pp 437–444.
- (2) (a) Kumalah Robinson, S. A.; Mempo, M. V. L.; Cairns, A. J.; Holman, K. T. A Cubic, 12-Connected, Microporous Metal-Organometallic Phosphate Framework Sustained by Truncated Tetrahedral Nodes. *J. Am. Chem. Soc.* **2011**, *133*, 1634–1637. (b) Lang, H.; Del Villar, A.; Walfort, B.; Rheinwald, G. Synthese und Reaktionsverhalten von Platin(II) und Kupfer(I) Koordinationspolymeren; die Festkörperstruktur von $\{trans-(\text{Ph}_3\text{P})_2\text{Pt}[(\eta^2-\text{C}\equiv\text{CPh})\text{CuBr}]_2\}_n$ und $trans-(\text{Ph}_3\text{P})_2\text{Pt}[(\eta^2-\text{C}\equiv\text{CPh})\text{CuNO}_3]_2$. *J. Organomet. Chem.* **2004**, *689*, 1464–1471. (c) Lang, H.; Del Villar, A.; Walfort, B. $\{trans-(\text{Ph}_3\text{P})_2\text{Pt}[(\mu-\sigma, \eta^2-\text{C}\equiv\text{CPh})\text{AgOTf}]_2\}_n$: a novel coordination polymer with Pt($\text{C}\equiv\text{CPh}$) $_2$ and Ag $[\mu-\text{OS}(\text{O})(\text{CF}_3)\text{O}]_2$ Ag linkages. *Inorg. Chem. Commun.* **2004**, *7*, 694–697.
- (3) (a) Chen, Y.; Sun, Q. Magnetic two-dimensional organic topological insulator: Au–1, 3, 5-triethynylbenzene framework. *J. Chem. Phys.* **2017**, *147*, 104704. (b) Kumalah, S. A.; Holman, K. T. Polymorphism and inclusion properties of three-dimensional metal-organometallic frameworks derived from a terephthalate sandwich compound. *Inorg. Chem.* **2009**, *48*, 6860–6872. (c) Vitillo, J. G.; Groppo, E.; Bordiga, S.; Chavan, S.; Ricchiardi, G.; Zecchina, A. Stability and reactivity of grafted $\text{Cr}(\text{CO})_3$ species on MOF linkers: a computational study. *Inorg. Chem.* **2009**, *48*, 5439–5448. (d) Oisaki, K.; Li, Q.; Furukawa, H.; Czaja, A. U.; Yaghi, O. M. A Metal-Organic Framework with Covalently Bound Organometallic Complexes. *J. Am. Chem. Soc.* **2010**, *132*, 9262–9264. (e) Pullen, S.; Fei, H.; Orthaber, A.; Cohen, S. M.; Ott, S. Enhanced photochemical hydrogen production by a molecular diiron catalyst incorporated into a metal–organic framework. *J. Am. Chem. Soc.* **2013**, *135*, 16997–17003.
- (4) Matassa, R.; Fratoddi, I.; Rossi, M.; Battocchio, C.; Caminiti, R.; Russo, M. V. Two-dimensional networks of Ag nanoparticles bridged by organometallic ligand. *J. Phys. Chem. C* **2012**, *116*, 15795–15800.
- (5) (a) Škoch, K.; Čísařová, I.; Schulz, J.; Siemeling, U.; Štěpnička, P. Synthesis and characterization of 1′-(diphenylphosphino)-1-isocyanoferrrocene, an organometallic ligand combining two different soft donor moieties, and its Group 11 metal complexes. *Dalton Trans.* **2017**, *46*, 10339–10354. (b) Gwengo, C.; Iyer, R.; Raja, M. Rational Design and Synthesis of a New Organometallic Ligand, 1-Ferrocenyl-3-(5-bromopyridyl)-prop-3-enol-1-one and Its Heteronuclear Coordination Polymer, $\{\text{Cu}[1\text{-ferrocenyl-3-(5-bromopyridyl)prop-1,3-dione}]_2\}_n$. *Cryst. Growth Des.* **2012**, *12*, 49–53. (c) Wei, K. J.; Ni, J.; Liu, Y. Heterobimetallic metal-complex assemblies constructed from the flexible arm-like ligand 1, 1′-bis [(3-pyridylamino) carbonyl] ferrocene: structural versatility in the solid state. *Inorg. Chem.* **2010**, *49*, 1834–1848. (d) Yang, Y. Y.; Wong, W. T. A novel 2-D interlinking zigzag-chain d–f mixed-metal coordination polymer generated from an organometallic ligand. *Chem. Commun.* **2002**, 2716–2717.
- (6) (a) Cooper, T. M.; Burke, A. R.; Krein, D. M.; Ziolo, R. F.; Arias, E.; Moggio, I.; Fratini, A.; Garbovskiy, Y.; Glushchenko, A. V. Cholesteric liquid crystal glass platinum acetylides. *MRS Online Proc. Libr.* **2014**, *1698*, 820. (b) Klövekorn, P.; Munch, J. Variable stimulated Brillouin scattering pulse compressor for nonlinear optical measurements. *Appl. Opt.* **1997**, *36*, 5913–5917. (c) Bruce, D. W.; Lea, M. S.; Marsden, J. R. The synthesis and mesomorphism of some acetylide complexes of platinum (II) and palladium (II). *Mol. Cryst. Liq. Cryst. Sci. Technol., Sect. A* **1996**, *275*, 183–194.
- (7) (a) Durand, R. J.; Gauthier, S.; Achelle, S.; Kahlal, S.; Saillard, J. Y.; Barsella, A.; Wojcik, L.; Le Poul, N.; Robin-Le Guen, F. Incorporation of a platinum center in the pi-conjugated core of push–pull chromophores for nonlinear optics (NLO). *Dalton Trans.* **2017**, *46*, 3059–3069. (b) Colombo, A.; Nisic, F.; Dragonetti, C.; Marinotto, D.; Oliveri, I. P.; Righetto, S.; Lobello, M. G.; De Angelis, F. Unexpectedly high second-order nonlinear optical properties of simple Ru and Pt alkynyl complexes as an analytical springboard for NLO-active polymer films. *Chem. Commun.* **2014**, *50*, 7986–7989. (c) Kindahl, T.; Öhgren, J.; Lopes, C.; Eliasson, B. Synthesis, optical power limiting, and DFT calculations of triplet–triplet absorption of three novel Pt (II)-diacetylide chromophores. *Tetrahedron Lett.* **2013**, *54*, 2403–2408. (d) Maiti, S. K.; Jardim, M. G.; Rodrigues, J.; Rissanen, K.; Campo, J.; Wenseleers, W. Divergent Route to the Preparation of Hybrid Pt–Fe 2, 4, 6-Tris (4-ethynyl) phenyl-1, 3, 5-triazine Metalloendrimers for Nonlinear Optics. *Organometallics* **2013**, *32*, 406–414. (e) Dubinina, G. G.; Price, R. S.; Abboud, K. A.; Wicks, G.; Wnuk, P.; Stepanenko, Y.; Drobizhev, M.; Rebane, A.; Schanze, K. S. Phenylene vinylene platinum (II) acetylides with prodigious two-photon absorption. *J. Am. Chem. Soc.* **2012**, *134*, 19346–19349. (f) Kindahl, T.; Ellingsen, P. G.; Lopes, C.; Brännlund, C.; Lindgren, M.; Eliasson, B. Photophysical and DFT characterization of novel Pt (II)-coupled 2, 5-diaxiazoles for nonlinear optical absorption. *J. Phys. Chem. A* **2012**, *116*, 11519–11530. (g) Chan, C. K. M.; Tao, C. H.; Li, K. F.; Wong, K. M. C.; Zhu, N.; Cheah, K. W.; Yam, V. W. W. Design, synthesis, characterization, luminescence and non-linear optical (NLO) properties of multinuclear platinum (II) alkynyl complexes. *Dalton Trans.* **2011**, *40*, 10670–10685. (h) Chan, C. K. M.; Tao, C. H.; Li, K. F.; Wong, K. M. C.; Zhu, N.; Cheah, K. W.; Yam, V. W. W. Synthesis, characterization, luminescence and

nonlinear optical (NLO) properties of truxene-containing platinum (II) alkynyl complexes. *J. Organomet. Chem.* **2011**, *696*, 1163–1173.

(8) (a) Goudreault, T.; He, Z.; Guo, Y.; Ho, C. L.; Zhan, H. M.; Wang, Q. W.; Ho, K. Y. F.; Wong, K. L.; Fortin, D.; Yao, B.; Xie, Z. Y.; Wang, L.; Kwok, W. M.; Harvey, P. D.; Wong, W. Y. Synthesis, Light-Emitting, and Two-Photon Absorption Properties of Platinum-Containing Poly(arylene-ethynylene)s Linked by 1,3-, -Oxadiazole Units. *Macromolecules* **2010**, *43*, 7936–7949. (b) Xu, L. J.; Zeng, X. C.; Wang, J. Y.; Zhang, L. Y.; Chi, Y.; Chen, Z. N. Phosphorescent PtAu₂ Complexes with Differently Positioned Carbazole–Acetylide Ligands for Solution-Processed Organic Light-Emitting Diodes with External Quantum Efficiencies of over 20%. *ACS Appl. Mater. Interfaces* **2016**, *8*, 20251–20257.

(9) (a) He, W.; Livshits, M. Y.; Dickie, D. A.; Yang, J.; Quinnett, R.; Rack, J. J.; Wu, Q.; Qin, Y. A “roller-wheel” Pt-containing small molecule that outperforms its polymer analogs in organic solar cells. *Chem. Sci.* **2016**, *7*, 5798–5804. (b) Siu, C. H.; Lee, L. T. L.; Yiu, S. C.; Ho, P. Y.; Zhou, P.; Ho, C. L.; Chen, T.; Liu, J.; Han, K.; Wong, W. Y. Synthesis and Characterization of Phenothiazine-Based Platinum (II)–Acetylide Photosensitizers for Efficient Dye–Sensitized Solar Cells. *Chem. - Eur. J.* **2016**, *22*, 3750–3757. (c) Gauthier, S.; Caro, B.; Robin-Le Guen, F.; Bhuvanesh, N.; Gladysz, J. A.; Wojcik, L.; Le Poul, N.; Planchat, A.; Pellegrin, Y.; Blart, E.; Jacquemin, D.; et al. Synthesis, photovoltaic performances and TD-DFT modeling of push–pull diacetylide platinum complexes in TiO₂ based dye-sensitized solar cells. *Dalton Trans.* **2014**, *43*, 11233–11242. (d) Tigreros, A.; Dhas, V.; Ortiz, A.; Insuasty, B.; Martín, N.; Echegoyen, L. Influence of acetylene-linked π -spacers on triphenylamine–fluorene dye sensitized solar cells performance. *Sol. Energy Mater. Sol. Cells* **2014**, *121*, 61–68. (e) Dai, F. R.; Zhan, H. M.; Liu, Q.; Fu, Y. Y.; Li, J. H.; Wang, Q. W.; Xie, Z.; Wang, L.; Yan, F.; Wong, W. Y. Platinum (II)–Bis(aryleneethynylene) Complexes for Solution-Processible Molecular Bulk Heterojunction Solar Cells. *Chem. - Eur. J.* **2012**, *18*, 1502–1511. (f) Wu, W.; Xu, X.; Yang, H.; Hua, J.; Zhang, X.; Zhang, L.; Long, Y.; Tian, H. D– π –M– π –A structured platinum acetylide sensitizer for dye-sensitized solar cells. *J. Mater. Chem.* **2011**, *21*, 10666–10671. (g) Zhan, H.; Lamare, S.; Ng, A.; Kenny, T.; Guernon, H.; Chan, W. K.; Djurišić, A. B.; Harvey, P. D.; Wong, W. Y. Synthesis and photovoltaic properties of new metalloporphyrin-containing poly-platinyne polymers. *Macromolecules* **2011**, *44*, 5155–5167. (h) Wang, Q.; He, Z.; Wild, A.; Wu, H.; Cao, Y.; S Schubert, U.; Chui, C. H.; Wong, W. Y. Platinum–acetylide polymers with higher dimensionality for organic solar cells. *Chem. - Asian J.* **2011**, *6*, 1766–1777.

(10) (a) Juvenal, F.; Bonnot, A.; Fortin, D.; Harvey, P. D. The *trans*-Bis(p-thioetherphenylacetyl) bis(phosphine) platinum (II) Ligands: A Step towards Predictability and Crystal Design. *ACS Omega* **2017**, *2*, 7433–7443. (b) Juvenal, F.; Langlois, A.; Bonnot, A.; Fortin, D.; Harvey, P. D. Luminescent 1D- and 2D-Coordination Polymers Using CuX Salts (X = Cl, Br, I) and a Metal-Containing Dithioether Ligand. *Inorg. Chem.* **2016**, *55*, 11096–11109.

(11) (a) Aloisi, A.; Berthet, J.-C.; Genre, C.; Thuery, P.; Cantat, T. Complexes of the tripodal phosphine ligands PhSi(XPPH₂)₃ (X = CH₂, O): synthesis, structure and catalytic activity in the hydroboration of CO₂. *Dalton Trans.* **2016**, *45*, 14774–14788. (b) Musina, E. I.; Shamsieva, A. V.; Strelnik, I. D.; Gerasimova, T. P.; Krivolapov, D. B.; Kolesnikov, I. E.; Grachova, E. V.; Tunik, S. P.; Bannwarth, C.; Grimme, S.; Katsyuba, S. A.; Karasik, A. A.; Sinyashin, O. G. Synthesis of novel pyridyl containing phospholanes and their polynuclear luminescent copper(I) complexes. *Dalton Trans.* **2016**, *45*, 2250–2260. (c) Karasik, A. A.; Musina, E. I.; Strelnik, I. D.; Balueva, A. S.; Budnikova, Y. H.; Sinyashin, O. G. Cyclic Phosphino Amino Pyridines–Novel Instrument for Construction of Catalysts and Luminescent Materials. *Phosphorus, Sulfur Silicon Relat. Elem.* **2015**, *190*, 729–732. (d) Siddiqui, M. M.; Mobin, S. M.; Senkovska, I.; Kaskel, S.; Balakrishna, M. S. Novel zeotype frameworks with soft cyclo-diphosphazane linkers and soft Cu₄X₄ clusters as nodes. *Chem. Commun.* **2014**, *50*, 12273–12276.

(12) SAINTE; Bruker AXS Inc.: Madison, WI, 2008.

(13) Frisch, M.; Trucks, G. W.; Schlegel, H.; Scuseria, G. E.; Robb, M. A.; Cheeseman, J. R.; Montgomery, J. A., Jr; Vreven, T. K. K. N.; Kudin, K. N.; Burant, J.; Millam, J. M. *Gaussian 03*, revision c. 02; Gaussian, Inc.: Wallingford, CT, 2004.

(14) Hohenberg, P.; Kohn, W. Inhomogeneous electron gas. *Phys. Rev.* **1964**, *136*, B864–871.

(15) Kohn, W.; Sham, L. J. Selfconsistent equations including exchange and correlation effects. *Phys. Rev.* **1965**, *140*, A1133.

(16) Parr, R. G.; Yang, W. *Density-functional theory of atoms and molecules*; Oxford University Press: Oxford, England, 1989.

(17) Salahub, D. R.; Zerner, M. C. The Challenge of d and f Electrons. *J. Am. Chem. Soc. Washington, D.C.* **1989**, *394*, 394.

(18) Bauernschmitt, R.; Ahlrichs, R. Treatment of electronic excitations within the adiabatic approximation of time dependent density functional theory. *Chem. Phys. Lett.* **1996**, *256*, 454–464.

(19) Casida, M. E.; Jamorski, C.; Casida, K. C.; Salahub, D. R. Molecular excitation energies to high-lying bound states from timedependent density-functional response theory: Characterization and correction of the time-dependent local density approximation ionization threshold. *J. Chem. Phys.* **1998**, *108*, 4439–4449.

(20) Stratmann, R. E.; Scuseria, G. E.; Frisch, M. J. An efficient implementation of time-dependent density-functional theory for the calculation of excitation energies of large molecules. *J. Chem. Phys.* **1998**, *109*, 8218–8224.

(21) Lee, C.; Yang, W.; Parr, R. G. Development of the Colic-Salvetti correlation-energy formula into a functional of the electron density. *Phys. Rev. B: Condens. Matter Mater. Phys.* **1988**, *37*, 785–789.

(22) Miehlich, B.; Savin, A.; Stoll, H.; Preuss, H. Results obtained with the correlation energy density functionals of Becke and Lee, Yang and Parr. *Chem. Phys. Lett.* **1989**, *157*, 200–206.

(23) Becke, A. D. Density-functional thermochemistry. III. The role of exact exchange. *J. Chem. Phys.* **1993**, *98*, 5648–5652.

(24) Binkley, J. S.; Pople, J. A.; Hehre, W. J. Self-consistent molecular orbital methods. 21. Small split-valence basis sets for first-row elements. *J. Am. Chem. Soc.* **1980**, *102*, 939–947.

(25) Gordon, M. S.; Binkley, J. S.; Pople, J. A.; Pietro, W. J.; Hehre, W. J. Self-consistent molecular-orbital methods. 22. Small split-valence basis sets for second-row elements. *J. Am. Chem. Soc.* **1982**, *104*, 2797–2803.

(26) Pietro, W. J.; Francl, M. M.; Hehre, W. J.; Defrees, D. J.; Pople, J. A.; Binkley, J. S. Self-consistent molecular orbital methods. 24. Supplemented small split-valence basis sets for second-row elements. *J. Am. Chem. Soc.* **1982**, *104*, 5039–5048.

(27) Dobbs, K. D.; Hehre, W. J. Molecular orbital theory of the properties of inorganic and organometallic compounds 4. Extended basis sets for third- and fourth-row, main-group elements. *J. Comput. Chem.* **1986**, *7*, 359–378.

(28) Dobbs, K. D.; Hehre, W. J. Molecular orbital theory of the properties of inorganic and organometallic compounds 5. Extended basis sets for first-row transition metals. *J. Comput. Chem.* **1987**, *8*, 861–879.

(29) Dobbs, K. D.; Hehre, W. J. Molecular orbital theory of the properties of inorganic and organometallic compounds. 6. Extended basis sets for second-row transition metals. *J. Comput. Chem.* **1987**, *8*, 880–893.

(30) O’Boyle, N. M.; Tenderholt, A. L.; Langner, K. M. Cclib: a library for package-independent computational chemistry algorithms. *J. Comput. Chem.* **2008**, *29*, 839–845.

(31) Sonogashira, K.; Fujikura, Y.; Yatake, T.; Toyoshima, N.; Takahashi, S.; Hagihara, N. Syntheses and properties of *cis*- and *trans*-dialkynyl complexes of platinum (II). *J. Organomet. Chem.* **1978**, *145*, 101–108. (b) Long, N. J.; White, A. J.; Williams, D. J.; Younus, M. Synthesis and characterisation of new platinum ethynyl dimers and polymers with pendant ferrocenyl groups. *J. Organomet. Chem.* **2002**, *649*, 94–99.

(32) Mukhopadhyay, S.; Lasri, J.; da Silva, M. F. C. G.; Charmier, M. A. J.; Pombeiro, A. J. Activation of C–CN bond of propionitrile: An alternative route to the syntheses of 5-substituted-1H-tetrazoles and dicyanoplatinum(II) species. *Polyhedron* **2008**, *27*, 2883–2888.

- (33) (a) Harvey, P. D.; Knorr, M. Designs of 3-Dimensional Networks and MOFs Using Mono- and Polymetallic Copper (I) Secondary Building Units and Mono- and Polythioethers: Materials Based on the Cu–S Coordination Bond. *J. Inorg. Organomet. Polym. Mater.* **2016**, *26*, 1174–1197. (b) Harvey, P. D.; Knorr, M. Stabilization of $(\text{CuX})_n$ Clusters (X = Cl, Br, I; n = 2, 4, 5, 6, 8) in Mono- and Dithioether-Containing Layered Coordination Polymers. *J. Cluster Sci.* **2015**, *26*, 411–459. (c) Harvey, P. D.; Knorr, M. Luminescent Coordination Polymers Built Upon Cu_4X_4 (X = Br, I) Clusters and Mono- and Dithioethers. *Macromol. Rapid Commun.* **2010**, *31*, 808–826.
- (34) (a) Song, Y.; Fan, R. Q.; Xing, K.; Du, X.; Su, T.; Wang, P.; Yang, Y. L. Insight into the Controllable Synthesis of Cu (I)/Cu (II) Metal–Organic Complexes: Size-Exclusive Selective Dye Adsorption and Semiconductor Properties. *Cryst. Growth Des.* **2017**, *17*, 2549–2559. (b) Zeng, G.; Xing, S.; Wang, X.; Yang, Y.; Xiao, Y.; Li, Z.; Li, G.; Shi, Z.; Feng, S. Synthesis, structures and luminescence properties of 3d–4f heterometallic–organic frameworks (HMOFs) constructed from different copper halide clusters. *CrystEngComm* **2016**, *18*, 4336–4342. (c) Zeng, G.; Xing, S.; Wang, X.; Yang, Y.; Ma, D.; Liang, H.; Gao, L.; Hua, J.; Li, G.; Shi, Z.; Feng, S. 3d–4f Metal–Organic Framework with Dual Luminescent Centers That Efficiently Discriminates the Isomer and Homologues of Small Organic Molecules. *Inorg. Chem.* **2016**, *55*, 1089–1095. (d) Zhang, Y.; Wu, T.; Liu, R.; Dou, T.; Bu, X.; Feng, P. Three-dimensional photoluminescent frameworks constructed from size-tunable CuI clusters. *Cryst. Growth Des.* **2010**, *10*, 2047–2049. (e) Bai, S. Q.; Kwang, J. Y.; Koh, L. L.; Young, D. J.; Hor, T. A. Functionalized 1, 2, 3-triazoles as building blocks for photoluminescent POLOs (polymers of oligomers) of copper (I). *Dalton Trans.* **2010**, *39*, 2631–2636. (f) Hou, Q.; Yu, J. H.; Xu, J. N.; Yang, Q. F.; Xu, J. Q. A new 3-D two-fold interpenetrated framework with sqp net based on Cu_6I_6 and Cu_8I_8 cluster nodes. *CrystEngComm* **2009**, *11*, 2452–2455. (g) Bi, M.; Li, G.; Hua, J.; Liu, Y.; Liu, X.; Hu, Y.; Shi, Z.; Feng, S. Two isomers with FSC topology constructed from $\text{Cu}_6\text{I}_6(\text{DABCO})_4$ and $\text{Cu}_8\text{I}_8(\text{DABCO})_6$ building blocks. *Cryst. Growth Des.* **2007**, *7*, 2066–2070. (h) Wang, J.; Zheng, S. L.; Hu, S.; Zhang, Y. H.; Tong, M. L. New in situ cleavage of both S–S and S–C (sp^2) bonds and rearrangement reactions toward the construction of copper (I) cluster-based coordination networks. *Inorg. Chem.* **2007**, *46*, 795–800. (i) Shan, X. C.; Zhang, H. B.; Chen, L.; Wu, M. Y.; Jiang, F. L.; Hong, M. C. Multistimuli-responsive luminescent material reversible switching colors via temperature and mechanical force. *Cryst. Growth Des.* **2013**, *13*, 1377–1381. (j) Bonnot, A.; Juvenal, F.; Lapprand, A.; Fortin, D.; Knorr, M.; Harvey, P. D. Can a highly flexible copper (I) cluster-containing 1D and 2D coordination polymers exhibit MOF-like properties? *Dalton Trans.* **2016**, *45*, 11413–11421. (k) Harvey, P. D.; Bonnot, A.; Lapprand, A.; Strohmman, C.; Knorr, M. Coordination $\text{RC}_6\text{H}_4\text{S}(\text{CH}_2)_8\text{SC}_6\text{H}_4\text{R}/(\text{CuI})_n$ Polymers (R(n) = H(4); Me(8)): An Innocent Methyl Group that Makes the Difference. *Macromol. Rapid Commun.* **2015**, *36*, 654–659.
- (35) Lapprand, A.; Bonnot, A.; Knorr, M.; Rousselin, Y.; Kubicki, M. M.; Fortin, D.; Harvey, P. D. Formation of an unprecedented $(\text{CuBr})_5$ cluster and a zeolite-type 2D-coordination polymer: a surprising halide effect. *Chem. Commun.* **2013**, *49*, 8848–8850.
- (36) (a) Kamei, T.; Fujita, K.; Itami, K.; Yoshida, J. I. Copper-catalyzed allylation of carbonyl derivatives using allyl (2-pyridyl) silanes. *Org. Lett.* **2005**, *7*, 4725–4728. (b) Itami, K.; Ushioji, Y.; Nokami, T.; Ohashi, Y.; Yoshida, J. I. Stereoselective Synthesis of Multisubstituted Butadienes through Directed Mizoroki–Heck Reaction and Homocoupling Reaction of Vinyl (2-pyridyl) silane. *Org. Lett.* **2004**, *6*, 3695–3698. (c) Filinchuk, Y. E.; Mys'kiv, M. G.; Davydov, V. N. -Complexation of Copper (I) with Allylacetone Oxime. Synthesis and Crystal Structure of the $\text{CuX}_2\text{C}_3\text{H}_5\text{-CH}_2\text{-C}(\text{CH}_3)=\text{N-OH}$ (X = Cl or Br) Compounds. *Russ. J. Coord. Chem.* **1998**, *24*, 722–726. (d) Luk'yanov, M. Y.; Pavlyuk, A. V.; Mys'kiv, M. G. π -Complexes of copper (I) halides with 3-(allylamino)- $(\text{C}_3\text{H}_5\text{NHC}_2\text{H}_4\text{CN}, \text{Apn})$ and 3-(diallylamino)- $((\text{C}_3\text{H}_5)_2\text{NC}_2\text{H}_4\text{CN}, \text{Dapn})$ -propanenitrile. Syntheses and crystal structures of compounds $[\text{CuCl}(\text{Apn})]$, $[(\text{H}^+ \text{Apn}) \text{Cu}_2\text{Cl}_3]$, $[(\text{H}^+ \text{Dapn}) \text{CuCl}_2]$, and $[(\text{H}^+ \text{Dapn}) \text{CuBr}_2]$. *Russ. J. Coord. Chem.* **2012**, *38*, 86–91. (e) Slyvka, Y.; Goresnik, E.; Veryasov, G.; Morozov, D.; Luk'yanov, M.; Mys'kiv, M. The first copper (I)-olefin complexes bearing a 1, 3, 4-oxadiazole core: Alternating-current electrochemical crystallization, X-ray experiment and DFT study. *Polyhedron* **2017**, *133*, 319–326.
- (37) Sabounchei, S. J.; Pourshahbaz, M.; Hashemi, A.; Ahmadi, M.; Karamian, R.; Asadbegy, M.; Khavasi, H. R. Synthesis and structural characterization of dimeric phosphine ylide Cu (I) complexes: Application in Suzuki cross-coupling reactions and biological evaluation as antibacterial agents. *J. Organomet. Chem.* **2014**, *761*, 111–119.
- (38) Sircoglou, M.; Bontemps, S.; Mercy, M.; Miquieu, K.; Ladeira, S.; Saffon, N.; Maron, L.; Bouhadir, G.; Bourissou, D. Copper (I) Complexes derived from Mono- and Diphosphino-Boranates: Cu→B Interactions Supported by Arene Coordination. *Inorg. Chem.* **2010**, *49*, 3983–3990.
- (39) Haider, J.; Kunz, K.; Scholz, U. Highly Selective Copper-Catalyzed Monoarylation of Aniline. *Adv. Synth. Catal.* **2004**, *346*, 717–722.
- (40) (a) Lobana, T. S.; Mahajan, R.; Castineiras, A. Metal-phosphine chalcogenide interactions. Crystal and molecular structures of $[\text{di-}\mu\text{-iodo-bis}\{(\text{methylcyanide-N})(\text{triphenylthiophosphorane-S})\text{copper(I)}\}]$ and $[\text{di-}\mu\text{-chloro-bis}\{\mu\text{-1,2-ethylenebis}(\text{diphenylphosphine selenide-Se,Se})\}\text{dicopper (I)}]$. *Transition Met. Chem.* **2001**, *26*, 440–444. (b) Johnson, N. A.; Wolfe, S. R.; Kabir, H.; Andrade, G. A.; Yap, G.; Heiden, Z. M.; Moberly, J. G.; Roll, M. F.; Waynant, K. V. Deconvoluting the Innocent vs. Non-Innocent Behavior of N, N-Diethylphenylazothioformamide Ligands with Copper Sources. *Eur. J. Inorg. Chem.* **2017**, *2017*, 5576–5581. (c) Munakata, M.; Wu, L. P.; Kuroda-Sowa, T.; Maekawa, M.; Suenaga, Y.; Nakagawa, S. One-, two- and three-dimensional copper (I) and silver (I) complexes of 2, 11-dithia [3.3] paracyclophane. *J. Chem. Soc., Dalton Trans.* **1996**, *0*, 1525–1530.
- (41) Lobana, T. S.; Verma, R.; Mahajan, R.; Tiekink, E. R. T. Crystal structure of $\text{di-}\mu\text{-iodo-bis}\{(\text{methylcyanide-N})(\text{triphenylselenophosphorane})\text{copper(I)}\}$, $[\text{CuI}(\text{Ph}_3\text{PSe})(\text{CH}_3\text{CN})_2]$. *Z. Kristallogr. - New Cryst. Struct.* **1999**, *214*, 513–514.
- (42) (a) Hadjidakou, S. K.; Antoniadis, S. D.; Aslanidis, P.; Cox, P. J.; Tsipis, A. C. An Exploration of the Structural and Bonding Variability in Mixed-Ligand Benzimidazole-2-thione (bromo)(triarylphosphane) dicopper(I) Complexes with Diamond-Shaped $\text{Cu}_2(\mu\text{-X})_2$ Core Structures. *Eur. J. Inorg. Chem.* **2005**, *2005*, 1442–1452. (b) Lobana, T. S.; Rekha; Butcher, R. J.; Castineiras, A.; Bermejo, E.; Bharatam, P. V. Bonding trends of thiosemicarbazones in mononuclear and dinuclear copper(I) complexes: syntheses, structures, and theoretical aspects. *Inorg. Chem.* **2006**, *45*, 1535–1542.
- (43) (a) Contreras, J. G.; Cortés, H. Polymeric coordination of 4, 4'-dithiodipridine with cobalt (II), nickel (II) and copper (II) halides. *Polyhedron* **1989**, *8*, 1545–1548. (b) Kuzelka, J.; Farrell, J. R.; Lippard, S. J. Modeling the syn disposition of nitrogen donors at the active sites of carboxylate-bridged diiron enzymes. Enforcing dinuclearity and kinetic stability with a 1, 2-diethynylbenzene-based ligand. *Inorg. Chem.* **2003**, *42*, 8652–8662.
- (44) (a) Yao, C.; Tian, Z.; Jin, D.; Zhao, F.; Sun, Y.; Yang, X.; Zhou, G.; Wong, W. Y. Platinum (II) acetylide complexes with star- and V-shaped configurations possessing good trade-off between optical transparency and optical power limiting performance. *J. Mater. Chem. C* **2017**, *5*, 11672–11682. (b) Lara, R.; Lalinde, E.; Moreno, M. T. Phosphorescent platinum (II) alkynyls end-capped with benzothiazole units. *Dalton Trans.* **2017**, *46*, 4628–4641. (c) Liu, Y.; Jiang, S.; Glusac, K.; Powell, D. H.; Anderson, D. F.; Schanze, K. S. Photophysics of monodisperse platinum-acetylide oligomers: Delocalization in the singlet and triplet excited states. *J. Am. Chem. Soc.* **2002**, *124*, 12412–12413.
- (45) Emmert, L. A.; Choi, W.; Marshall, J. A.; Yang, J.; Meyer, L. A.; Brozik, J. A. The excited-state symmetry characteristics of platinum phenylacetylene compounds. *J. Phys. Chem. A* **2003**, *107*, 11340–11346.

(46) An, M.; Yan, X.; Tian, Z.; Zhao, J.; Liu, B.; Dang, F.; Yang, X.; Wu, Y.; Zhou, G.; Ren, Y.; Gao, L. Optimized trade-offs between triplet emission and transparency in Pt (II) acetylides through phenylsulfonyl units for achieving good optical power limiting performance. *J. Mater. Chem. C* **2016**, *4*, 5626–5633.

(47) (a) Cooper, T. M.; Haley, J. E.; Krein, D. M.; Burke, A. R.; Slagle, J. E.; Mikhailov, A.; Rebane, A. Two-Photon Spectroscopy of a Series of Platinum Acetylides: Conformation-Induced Ground-State Symmetry Breaking. *J. Phys. Chem. A* **2017**, *121*, 5442–5449. (b) Lin, C. J.; Chen, C. Y.; Kundu, S. K.; Yang, J. S. Unichromophoric platinum-acetylides that contain pentiptycene scaffolds: Torsion-induced dual emission and steric shielding of dynamic quenching. *Inorg. Chem.* **2014**, *53*, 737–745.

(48) Marineau-Plante, G.; Juvenal, F.; Langlois, A.; Fortin, D.; Soldera, A.; Harvey, P. D. Multiply “trapped” $^3[trans-Pt(PR_3)_2(C\equiv CC_6H_4X)_2]^*$ conformers in rigid media. *Chem. Commun.* **2018**, *54*, 976–979.